

POSSIBLE AGN SHOCK HEATING IN THE COOL CORE GALAXY CLUSTER ABELL 478

ALASTAIR J. R. SANDERSON¹, ALEXIS FINOGUENOV², AND JOSEPH J. MOHR^{1,3}

1) Department of Astronomy, University of Illinois, Urbana, IL 61801

2) Max-Planck-Institut für extraterrestrische Physik, Giessenbachstraße, 85748 Garching, Germany and

3) Department of Physics, University of Illinois, Urbana, IL 61801

Accepted by ApJ

ABSTRACT

We present a detailed X-ray study of the intracluster medium (ICM) of the nearby, cool-core galaxy cluster Abell 478 ($z = 0.088$), based on *Chandra* and *XMM-Newton* observations. Using a wavelet smoothing hardness analysis, we derive detailed temperature maps of A478, revealing a surprising amount of temperature structure for an apparently well relaxed cluster. We find the broad band *Chandra* spectral fits yield temperatures which are significantly hotter than those obtained with *XMM-Newton*, but the Fe ionization temperature shows good agreement. We show that the temperature discrepancy is slightly reduced when comparing spectra from regions selected to enclose nearly isothermal gas. However, by simulating multi-temperature spectra and fitting them with a single temperature model, we find no significant difference between *Chandra* and *XMM-Newton*, indicating that non-isothermality cannot fully explain the discrepancy.

We have discovered four hot spots located between 30–50 kpc from the cluster center, where the gas temperature is roughly a factor of 2 higher than in the surrounding material. We estimate the combined excess thermal energy present in these hot spots to be $(3 \pm 1) \times 10^{59}$ erg. The location of and amount of excess energy present in the hot spots are suggestive of a common origin within the cluster core, which hosts an active galactic nucleus. This cluster also possesses a pair of X-ray cavities coincident with weak radio lobes, as reported in a previous analysis, with an associated energy of less than 10% of the thermal excess in the hot spots. The presence of these hot spots could indicate strong-shock heating of the intracluster medium from the central radio source – one of the first such detections in a cool core cluster. Using the high resolution of *Chandra*, we probe the mass distribution in the core and find it to be characterized by a logarithmic slope of -0.35 ± 0.22 , which is significantly flatter than an NFW cusp of -1 and consistent with recent strong lensing results for a number of clusters.

Subject headings: galaxies: clusters: individual (A478) – cosmology: observation – galaxies: clusters: general – X-rays: galaxies: clusters

1. INTRODUCTION

Clusters of galaxies are critical sites for investigating the interaction between galaxies and their environment – particularly their impact upon the gaseous intracluster medium (ICM). There is substantial evidence to demonstrate that the ICM has been subjected to non-gravitational heating and/or cooling, so as to break the simple, self-similar scaling of cluster properties with mass; e.g. the $L - T_X$ (e.g. Edge & Stewart 1991; Arnaud & Evrard 1999; Fairley et al. 2000), $M_{\text{gas}} - T_X$ (Mohr, Mathieson, & Evrard 1999) and isophotal size-temperature (Mohr & Evrard 1997) relations. Furthermore, it is apparent that the ICM is systematically under-dense and more extended in less massive halos (e.g. Ponman, Cannon, & Navarro 1999; Sanderson et al. 2003; Osmond & Ponman 2004; Afshordi, Lin, & Sanderson 2005), and there is an increasing excess of entropy in the gas in cooler systems (Ponman, Sanderson, & Finoguenov 2003).

While these observations can be explained by the impact of feedback associated with galaxy formation (e.g. Voit & Ponman 2003), the precise details of the mechanisms which mediate this interaction remain unknown. Of critical importance is the role of radiative cooling, which could fuel star formation and gradually deplete the reservoir of gas in the cluster core. Despite the inherently unstable nature of cooling by thermal bremsstrahlung, gas in the dense, undisturbed cores of galaxy clusters appears not to be cooling at the expected level (e.g. Tamura et al. 2001; Peterson et al. 2003;

Kaastra et al. 2004), leading to greatly reduced mass deposition rates (Makishima et al. 2001; Böhringer et al. 2002). A plausible explanation for this behaviour is that thermal conduction acts to transfer significant amounts of energy from the outer regions of the ICM (Kim & Narayan 2003; Voigt & Fabian 2004). However, this process cannot operate at all (Khosroshahi, Jones, & Ponman 2004) or effectively enough (e.g. Wise, McNamara, & Murray 2004) to heat the core in all cases, especially at lower temperatures.

Since many “cooling flow” clusters are known to harbor central radio sources (Burns 1990; Eilek 2004), it is likely that active galactic nuclei (AGN) can deposit energy directly into the ICM, and thus offset at least some of the cooling. Recently, Croston, Hardcastle, & Birkinshaw (2005) have demonstrated that heating from low power radio galaxies could account for the steepening of the $L - T_X$ relation in X-ray bright galaxy groups. Although clusters are much more massive, the amount of energy output by powerful radio sources is certainly sufficient to heat the gas by the required amount (Churazov et al. 2002); what is lacking is a clear understanding of exactly how this energy is coupled to the ICM.

A number of clusters have been shown to possess cavities, where expanding radio lobes have displaced the ambient medium and left a depression in the projected X-ray surface brightness (e.g. see the compilation of Bîrzan et al. 2004, and references therein). However, the coolest gas is generally found beside these lobes (Fabian et al. 2000; McNamara et al. 2001) and their essentially subsonic expansion is not obviously heating the ICM by a significant amount. In the mean-

time, the role of AGN driven bubbles in modifying the ICM is opening up as a very promising avenue of research (see Gardini & Ricker 2004, for a recent review).

Alternatively, energy may be transferred to the ICM by means of acoustic waves generated by turbulence (Fujita, Suzuki, & Wada 2004), or viscous dissipation of sound waves originating from a central radio source (Ruszkowski et al. 2004a,b). Fabian et al. (2003) have recently discovered ripples in the X-ray emission from the Perseus Cluster, which point to a continuous energy output from the central radio source that can balance cooling within the innermost 50 kpc of the core.

In this paper we examine in detail the properties of the ICM in a nearby galaxy cluster, using X-ray data from two different telescopes. This apparently well relaxed system has a large cool core and its central galaxy hosts an active radio source, affording an excellent opportunity to study its interaction with the ICM. We assume the following cosmological parameters: $H_0 = 70 \text{ km s}^{-1} \text{ Mpc}^{-1}$, $\Omega_m = 0.3$, $\Omega_\Lambda = 0.7$. Correspondingly, at our adopted redshift for A478 of 0.088, $1'' = 1.65 \text{ kpc}$. Throughout our spectral analysis we have used XSPEC 11.3.0, incorporating the default solar abundance table of Anders & Grevesse (1989). All errors are 1σ , unless otherwise stated.

2. DATA REDUCTION

2.1. *Chandra* X-ray Data Reduction

A 42.4 ks *Chandra* observation of Abell 478 was made on January 29, 2001 using the Advanced CCD Imaging Spectrometer (ACIS) in FAINT mode. The data reduction and analysis were performed with Ciao version 3.0.2 and CALDB version 2.26. This release of the *Chandra* CALDB calibration files was the first to incorporate a full correction for the degradation in quantum efficiency of the ACIS detectors. Therefore, no further steps were taken to correct for its effects.

Three separate light curves were constructed for the S1, S3 and the remaining CCDs combined, using the recommended energy and time binning criteria¹. A small flare was identified in the light curve from the S1 CCD and another was found in the combined I2/I3/S2/S4 light curve: both were excluded, leaving 40.7 ks of useful data. Only events with ASCA grades 0,2,3,4,6 were used, and bad columns and hot pixels were excluded. In addition, those events associated with cosmic ray afterglows were identified and removed. A correction was applied to the level 1 events file to allow for the ACIS time-dependent gain variation, using the tool “corr_tgain”², and a new level 2 events file was generated by reprocessing this modified level 1 events dataset.

Since A478 fills much of the *Chandra* field of view, we use the Markevitch blank-sky datasets to estimate the background contribution³. To allow for small variations in the particle background level between the blank sky fields and the A478 observation, we rescaled the effective exposure of the background datasets according to the ratio of count rates in the particle-dominated 7–12 keV energy band for the S1 CCD, which is furthest away from the cluster. To avoid the bias caused by the presence of contaminating point sources in the A478 dataset, we identified and excluded such features using the following iterative scheme.

Images were extracted in the 0.5–2.0 keV band for the S1

CCD in both the main (A478) and blank sky datasets. A background image was created by smoothing the blank sky field with a Gaussian of width 1 arcmin, to filter out Poisson noise. The main image was then searched for sources with the ciao task WAVDETECT, using this background. The source regions found were then masked out of both the main and blank sky datasets, and the remaining counts in the 7–12 keV band were summed. A rescale factor was then determined as the ratio of the net count rate in the background dataset to that in the main dataset. The effective exposure time of the blank sky dataset was then multiplied by this rescale factor and the process repeated, until no new source regions were found. A total of 6 contaminating source regions were identified and excluded from the S1 CCD data in this way. We found that the blank sky data were 8% higher than in the A478 observation, consistent with the value of 10% quoted by Sun et al. (2003, hereafter S03) for the same observation.

2.2. *XMM* X-ray Data Reduction

XMM-Newton observed A478 in orbit 401 (observation ID 0109880101), using the thin filter to block visible light. In the analysis that follows we present the data obtained with the pn-CCD camera (Strüder & et al. 2001), operated in extended full-frame mode, with an exposure time of 42 ks. The initial stages of the data reduction were performed using XMMSAS 5.4.1. Screening of the data for contamination from flares was achieved by examining a light curve of detector counts in the 10–15 keV band. We have adopted the approach based on the analysis of the count rate histogram, as described in Zhang et al. (2004), which is more sensitive to the background conditions during the observations than using a fixed threshold to identify good time intervals.

With these screened photon event files we produced a pn image of A478 in the energy bands 0.5–2.0 and 2.0–7.5 keV. In the imaging analysis, we included photons near the pn-CCD borders, near bad pixels and offset columns, in order to reduce the width of the gaps between CCD chips. This is a reasonable approach to adopt when dealing with qualitative images in broad energy bands. For the spectral fitting, described in §3, we exclude all these border events, since a small fraction of those photons have an incorrect energy, typically due to the registration of a double event pattern as a single event. After subtracting the expected out-of-time events from the image, we corrected the residual for vignetting and exposure using the latest calibrations (Lumb et al. 2003), which have been incorporated within the XMMSAS 6.0 release.

Emission from A478 fills the entire *XMM-Newton* field of view and so it was not possible to determine the background level reliably from this dataset. Therefore, an observation of the *Chandra* Deep Field South was used to provide an estimate of the background. We have confirmed that this choice of dataset is well matched to the detector background in the 10–15 keV band for our observation of A478. However, for the goal of the current analysis the choice of the background is less important, since the measured flux is strongly dominated by emission from the cluster.

3. CHANDRA SPECTRAL ANALYSIS

A global spectrum of A478 was extracted from the emission filling the entire S3 chip, excluding contaminating sources. The spectrum was grouped to a minimum of 20 counts per bin, to enable us to use the χ^2 fit statistic. The CCD detector responses vary as a function of position within our spectral extraction region. We therefore generated composite response

¹ <http://cxc.harvard.edu/contrib/maxim/bg>.

² http://asc.harvard.edu/cont-soft/software/corr_tgain.1.0.html

³ <http://cxc.harvard.edu/contrib/maxim/acisbg>.

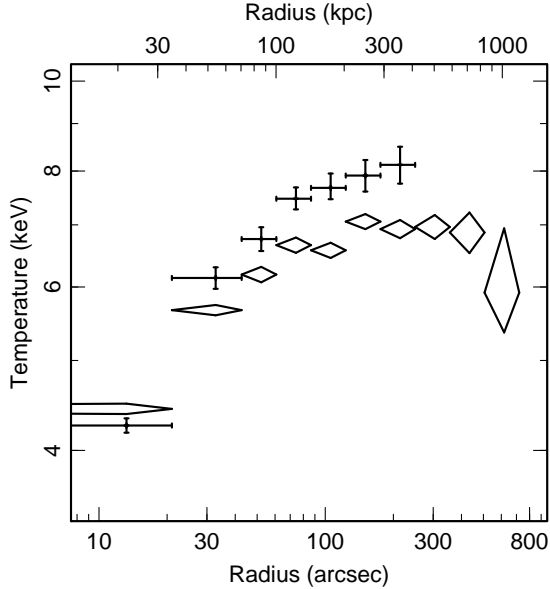


FIG. 1.— Projected gas temperature as a function of radius. The diamonds are the *XMM-Newton* pn data and the barred crosses are the *Chandra* data.

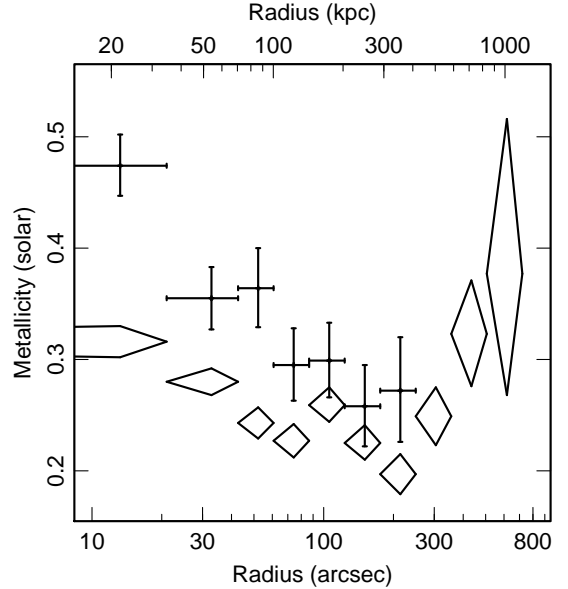


FIG. 2.— Projected gas metallicity as a function of radius. The diamonds are the *XMM-Newton* pn data and the barred crosses are the *Chandra* data.

files using the CIAO tasks MKWARF and MKRMF, by averaging the contributions made from those parts of the detector with different responses, weighting each component according to the distribution of counts in the 0.5–2.0 keV band.

Using XSPEC 11.3.0, a single temperature MEKAL hot plasma model combined with a WABS galactic absorption component, was fitted to the data between 0.7 and 7.0 keV, to maximize the signal-to-noise ratio (S/N). This yielded a best-fit temperature of 6.56 ± 0.06 keV, with a metallicity of 0.33 ± 0.01 solar, and an absorbing column of $(2.91 \pm 0.01) \times 10^{21}$ cm $^{-2}$. The redshift was also left free to vary, giving a best-fit value of $0.0879^{+0.0003}_{-0.0012}$, which agrees well with the optical value of 0.0881 ± 0.0009 (Struble & Rood 1999). We note that S03 found the following spectral parameters based on their 0.7–8.0 keV analysis of data from the S2, S3 & S4 CCDs combined using this observation: $kT = 7.18 \pm 0.11$ and $N_H = (2.59 \pm 0.03) \times 10^{21}$ cm $^{-2}$, with an abundance of 0.37 ± 0.02 solar (all at 90% confidence). The differences are not surprising, since the gas temperature shows a marked decrease in the cluster center and the metallicity and absorbing column both exhibit central enhancements (see §3.1) beyond the S3 chip, to which we restrict our analysis. However, the significant discrepancy in absorbing column is mainly due to the improvement in the *Chandra* calibration since the Sun et al. analysis – a factor which we will return to in Section 4.

3.1. *Chandra* vs *XMM*

In view of our intention to exploit the complementary properties of *Chandra* and *XMM-Newton*, by combining spectral data from both (see §4), we present here a detailed comparison of results obtained from the two observatories. We are further motivated by the apparent discrepancy between the temperatures inferred from *Chandra* and *XMM-Newton* observations of A478, as reported by Pointecouteau et al. (2004). Given the potential for spatial variation in cluster gas properties (as well as in the absorbing column), we perform a direct comparison of spectral properties in a series of contiguous annuli.

Ten logarithmically-spaced radial bins were defined out to a maximum radius of 12' (see Table 1), centered on the peak of the emission as measured using *Chandra* (R.A. 04^h13^m25^s.2, decl. 10°27'53''). The innermost bin radius was increased to 21'', to reduce the effect of scattering between bins, due to the comparatively broad point spread function (PSF) of *XMM-Newton*. Equivalent *Chandra* spectra were extracted in the 7 innermost annuli fully covered by the S3 chip.

Absorbed MEKAL models were fitted to each spectrum, as before, and radial profiles of temperature, metallicity and absorbing column are plotted in Figs. 1–3, respectively, showing the *Chandra* data as barred crosses and the *XMM-Newton* data as diamonds. The temperature profile is typical of a ‘cool-core’ cluster, showing a sharp drop towards the center, within $\sim 1'$. The region outside the core is roughly isothermal, with some indication of a negative gradient further out. It is also clear that the *Chandra* points are systematically higher in temperature compared to *XMM-Newton*. This discrepancy persists in the measured abundances, with *Chandra* again giving somewhat higher values than *XMM-Newton* in all annuli (Fig. 2). Nonetheless, both observations show an increase in the gas metallicity in the cluster core, approximately coincident with the observed decrease in temperature in this region. Vikhlinin et al. (2004) present a recent analysis of the A478 *Chandra* data, which incorporates the latest calibration. Their projected temperature profile is similar to our own, although it extends beyond the S3 chip, reaching a slightly hotter peak of ~ 9 keV at roughly 150 arcsec.

Furthermore, the inferred absorption column also rises towards the center, and there is close agreement between the *Chandra* and *XMM-Newton* results (Fig. 3). Also plotted is the galactic absorption of 1.51×10^{21} cm $^{-2}$ based on HI observations (Dickey & Lockman 1990) interpolated to the center of A478. It can be seen that the fitted points lie well above this line, implying an observed absorption roughly twice as high. However, this excess is not localized to the cluster core, and is probably associated with absorption in our galaxy (Pointecouteau et al. 2004). This behavior is not un-

TABLE 1
SPECTRAL FITTING RESULTS (0.7–7.0 keV)

<i>Chandra</i>				<i>XMM-Newton</i>				
R_{out}^a (")	kT (keV)	Z (solar)	nH (10^{21} cm $^{-2}$)	χ^2/dof	kT (keV)	Z (solar)	nH (10^{21} cm $^{-2}$)	χ^2/dof
21	4.25 ± 0.08	0.47 ± 0.03	2.98 ± 0.06	459.8 / 346	4.43 ± 0.06	0.32 ± 0.01	2.87 ± 0.04	1367.8 / 1006
43	6.14 ± 0.16	0.35 ± 0.03	2.86 ± 0.05	434.7 / 376	5.67 ± 0.07	0.28 ± 0.01	2.83 ± 0.04	1456.2 / 1150
61	6.76 ± 0.20	0.36 ± 0.04	2.81 ± 0.06	415.3 / 357	6.19 ± 0.12	0.24 ± 0.01	2.76 ± 0.04	1312.2 / 1083
87	7.47 ± 0.20	0.29 ± 0.03	2.76 ± 0.06	437.6 / 374	6.66 ± 0.13	0.23 ± 0.01	2.71 ± 0.04	1197.7 / 1095
123	7.67 ± 0.28	0.30 ± 0.03	2.74 ± 0.06	455.3 / 379	6.57 ± 0.12	0.26 ± 0.02	2.69 ± 0.04	1325.2 / 1096
175	7.91 ± 0.31	0.26 ± 0.04	2.64 ± 0.06	443.5 / 385	7.06 ± 0.13	0.23 ± 0.02	2.62 ± 0.04	1189.4 / 1116
250	8.12 ± 0.37	0.27 ± 0.05	2.67 ± 0.07	454.1 / 379	6.93 ± 0.16	0.20 ± 0.02	2.57 ± 0.05	1039.3 / 1058
355	6.96 ± 0.21	0.25 ± 0.03	2.20 ± 0.06	1025.5 / 1002
506	6.87 ± 0.35	0.32 ± 0.05	2.18 ± 0.11	1095.8 / 975
720	5.92 ± 0.57	0.38 ± 0.11	2.40 ± 0.25	1035.0 / 1030

NOTE. — ^aOuter radius of annulus. The redshift was fixed at 0.088 for all spectra. All errors are 1σ .

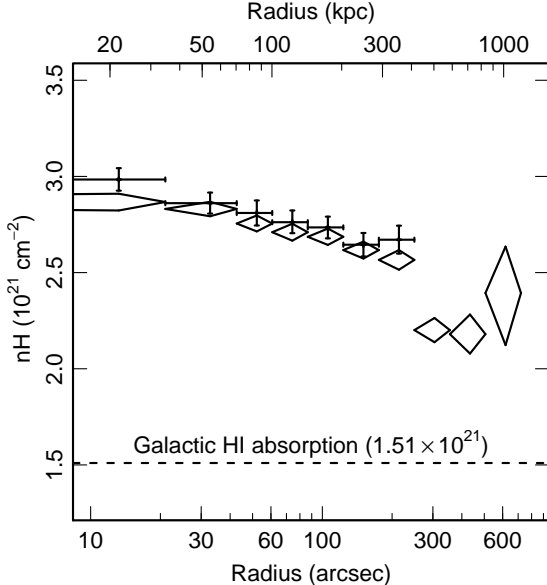


FIG. 3.— Projected absorbing column as a function of radius. The diamonds are the *XMM-Newton* pn data and the barred crosses are the *Chandra* data. The HI inferred absorption value is indicated by the dotted line.

expected, since HI measurements become an increasingly unreliable predictor of the total galactic absorption for columns exceeding $\sim 6 \times 10^{20}$ cm $^{-2}$ due to contributions from molecular hydrogen, for example (Lockman 2004). An excess absorption was also inferred from photometric observations by Garilli et al. (1996), who noted that the early-type galaxies in A478 are much redder than expected.

In light of the disagreement in both temperature and metallicity between *Chandra* and *XMM-Newton*, we performed additional tests to verify the impact of any calibration errors on our results. Specifically, we checked the ionization temperature of the ICM, as measured from the prominent iron line redshifted to ~ 6.1 keV in the observer frame. We extracted a spectrum from annuli 4–7 combined, thus excluding the inner cluster core, which contains gas at a wide range of temperatures and metallicities, as already seen. This spectrum was fitted with an absorbed MEKAL model as before, in the ranges 0.7–7.0 keV and 6.0–6.8 keV (see Fig. 4). Since the absor-

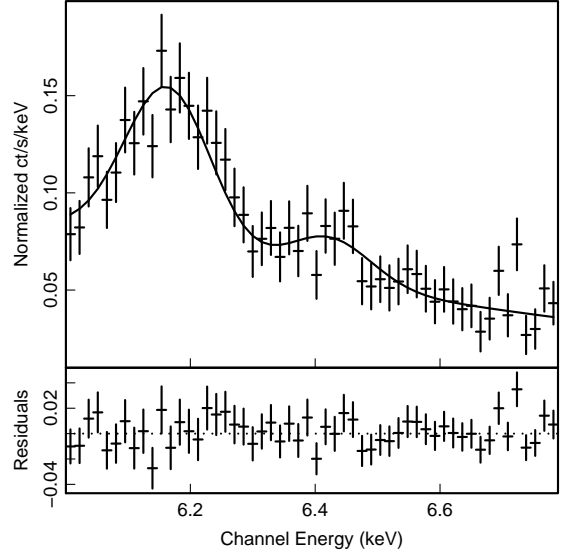


FIG. 4.— The 6.0–6.8 keV ACIS spectrum, best fitting MEKAL model and residuals from annuli 4–7 combined (see text for details).

ing column was poorly constrained when fitting the narrow (high) energy range, we fixed it at the value obtained from the 0.7–7.0 keV fit. However, we also tried fixing N_{H} at the galactic value deduced from HI observations (1.51×10^{21} cm $^{-2}$). This made no appreciable difference to the results, which are summarized in the left half of Table 2. The corresponding χ^2 and degrees of freedom are (711.07/427) and (39.49/51), for the broad and narrow range *Chandra* fits, respectively. It is clear from the broad band fit that, even within this apparently roughly isothermal region, the cluster emission is not well described by a single temperature plasma. This hints at the presence of significant spatial variation in the temperature of the ICM – a possibility which we investigate further in §5.3.

For direct comparison, the equivalent test was performed on the *XMM-Newton* pn spectrum from annuli 4–7; the results are summarized in the right hand side of Table 2. As with *Chandra*, it was necessary to fix N_{H} for the narrow band fit at the optimum value obtained from the 0.7–7.0 keV fit. Once again we checked that the results do not change noticeably when N_{H} was fixed at the HI value. However, we did find that

TABLE 2
SPECTRAL FITTING RESULTS FOR ANNULI 4–7 COMBINED

<i>Chandra</i>					<i>XMM-Newton</i>			
Fit Range (keV)	<i>kT</i> (keV)	<i>Z</i> (solar)	<i>nH</i> (10 ²¹ cm ⁻²)	χ^2/dof	<i>kT</i> (keV)	<i>Z</i> (solar)	<i>nH</i> (10 ²¹ cm ⁻²)	χ^2/dof
0.7–7.0	7.73 ± 0.15	0.28 ± 0.02	2.72 ± 0.03	711.1 / 427	6.81 ± 0.06	0.28 ± 0.01	2.66 ± 0.02	1338.0 / 1256
6.0–6.8	6.49 ± 0.61	0.22 ± 0.05	2.72 (frozen)	39.5 / 51	6.69 ± 0.26	0.24 ± 0.02	2.66 (frozen)	158.5 / 152

NOTE. — The redshift was fixed at 0.088 for *Chandra*, but left free to vary for the *XMM-Newton*, broad-band fit; a simple linear gain offset was fitted to the narrow-band *XMM-Newton* spectrum to give the correct redshift (see text for details). All errors are 1 σ .

freezing the redshift at the optical value of 0.088 produced an unacceptable fit ($\chi^2/\text{dof} = 423.20/154$), indicative of a small calibration offset, also found by Pointecouteau et al. (2004) and de Plaa et al. (2004). This is due to the uncertainty in the current CTI correction affecting the pn detector in extended full frame mode only (K. Dennerl 2004, private communication), a correction for which has only just been incorporated into the XMMSAS 6.1 release. Leaving the redshift free to vary produced a best-fit value of 0.074 ± 0.001 . To provide a fairer comparison with *Chandra* in a region heavily dominated by emission line flux, we therefore applied a small modification to the response matrix file to improve the fit, using the XSPEC “gain” command. This produced an acceptable fit with a χ^2/dof of (158.65/154), compared to (1337.99/1261) for the broad range fit, without the gain modification. The 2 fitted gain parameters were frozen at their best fit values in the calculation of MEKAL parameter errors.

Table 2 shows that the broad-band *Chandra* spectrum produces an anomalously high temperature, which disagrees with the *Chandra* ionization temperature measurement, as well as with both the broad-band and ionization temperature fits from *XMM-Newton*. This could indicate a problem with the ACIS calibration as the source of the discrepancy between *Chandra* and *XMM-Newton* reported by Pointecouteau et al. (2004) and seen in Table 2, for this dataset. However, this behavior can be explained by significant temperature variation within each annulus, giving rise to different characteristic average temperatures when folded through the *Chandra* and *XMM-Newton* responses and fit with a single phase plasma model (see §5.3). The implication is that better agreement between *Chandra* and *XMM-Newton* ought to occur for spectra extracted from approximately isothermal regions, which we find to be the case (see §5.3).

In the meantime, we have neglected to correct for this bias in what follows, in view of the impracticality of restricting our *Chandra* analysis to a small, high energy range, and given the somewhat better agreement between *Chandra* and *XMM-Newton* seen in the deprojected temperature profile (see §4).

3.2. The Effects of Multiphase Gas

In order to shed some light on the discrepancy between *Chandra* and *XMM-Newton* described above, we have conducted a series of simulations of multiphase spectra, which we have fitted with a single temperature spectrum. We have used the spectral responses and background spectrum from annuli 4–7 (see Table 2) for both telescopes and assumed a value of galactic absorption of $2.7 \times 10^{21} \text{ cm}^{-2}$ for all these simulations. Initially we generated 1000 realisations of a spectrum comprising 4 temperature components (6,6.5,7.5 & 8 keV, weighted in the ratio 7:10:30:7), with an abundance of 0.3 solar. The results of fitting this spectrum with a single ab-

sorbed MEKAL model recovered the following mean temperatures and standard deviations: 7.11 ± 0.10 (*Chandra* 0.7–7.0 keV); 7.12 ± 0.06 (*XMM* 0.7–7.0 keV); 7.16 ± 0.45 (*Chandra* 6.0–6.8 keV); 7.17 ± 0.19 (*XMM* 6.0–6.8 keV). The excellent agreement between these 4 cases demonstrates that moderately multiphase gas with the same metallicity cannot account for the discrepancies seen in Table 2, despite the differences in the spectral responses for *Chandra* and *XMM-Newton*.

We then simulated a spectrum with 2 temperature components (5 and 12 keV) and an abundance of 0.3 solar (case A), 0.2 & 0.5 solar (case B), and 0.5 & 0.2 solar (case C), respectively. The fitting results are summarised in Table 3. It can be seen that there is consistently good agreement between *Chandra* and *XMM-Newton* in all 3 cases. Furthermore, it can also be seen that the 0.7–7.0 and 6.0–6.8 results are generally in good agreement when both have the same metallicity. However, when the hotter phase has higher metallicity, the narrow-band ionization balance fit yields a significantly hotter temperature for both *Chandra* and *XMM-Newton*. Conversely, when the cooler phase is more enriched, the 6.0–6.8 keV fit yields a cooler temperature, albeit at rather lower significance.

As an aside we note that, in all cases, the metallicity obtained with a single-temperature fit to the multiphase spectra overestimates the input values, by $\sim 25\%$ in the simple case where the 2 phase have the same abundance. Where the metallicities of the 2 phases differ, the abundance is over-estimated by an even greater amount, for both the broad- and narrow-band fits.

Based on these simulations, we therefore conclude that the discrepancy we observe between *Chandra* and *XMM-Newton* cannot readily be explained by the presence of multiple temperature components, even with differing abundances.

4. DEPROJECTION ANALYSIS

To determine the intracluster gas properties, we implemented a standard “onion peeling” scheme to deproject the X-ray data, under the assumption of spherical symmetry. The spectral deprojection was performed using the PROJCT model in XSPEC, using a single-temperature MEKAL plasma model with a galactic absorption component (WABS). Only data within 0.7 and 7.0 keV were used, and each spectrum was grouped to a minimum of 20 counts per bin, including the background contribution. The foreground absorbing column density was left free to vary in each annulus, as was the MEKAL temperature, abundance and normalization.

The XSPEC MEKAL normalization is defined as

$$K = \frac{10^{-14}}{4\pi(D_A(1+z))^2} \int n_e n_H dV, \quad (1)$$

where D_A is the angular diameter distance, z is the redshift and dV is the volume from which the deprojected emission

TABLE 3
SPECTRAL FITTING RESULTS FOR SIMULATED MULTIPHASE SPECTRA

Sim.	Fit Range (keV)	<i>Chandra</i>					<i>XMM-Newton</i>				
		<i>kT</i> (keV)	<i>Z</i> (solar)	<i>nH</i> (10^{21} cm $^{-2}$)	χ^2/dof	<i>kT</i> (keV)	<i>Z</i> (solar)	<i>nH</i> (10^{21} cm $^{-2}$)	χ^2/dof		
A	0.7–7.0	7.28 ± 0.12	0.37 ± 0.02	2.66 ± 0.03	439.1 / 427	7.36 ± 0.06	0.38 ± 0.01	2.65 ± 0.02	1294.6 / 1260		
A	6.0–6.8	7.65 ± 0.63	0.39 ± 0.08	2.70 (frozen)	51.8 / 51	7.70 ± 0.28	0.39 ± 0.04	2.70 (frozen)	157.7 / 155		
B	0.7–7.0	7.50 ± 0.15	0.38 ± 0.03	2.65 ± 0.04	443.4 / 427	7.67 ± 0.09	0.39 ± 0.01	2.61 ± 0.02	1324.4 / 1260		
B	6.0–6.8	9.19 ± 0.57	0.54 ± 0.10	2.70 (frozen)	51.5 / 51	9.16 ± 0.22	0.53 ± 0.04	2.70 (frozen)	156.9 / 155		
C	0.7–7.0	7.03 ± 0.11	0.49 ± 0.03	2.67 ± 0.03	455.7 / 427	7.07 ± 0.06	0.48 ± 0.01	2.67 ± 0.02	1331.4 / 1260		
C	6.0–6.8	6.45 ± 0.53	0.41 ± 0.08	2.70 (frozen)	51.5 / 51	6.46 ± 0.24	0.39 ± 0.04	2.70 (frozen)	157.6 / 155		

NOTE. — Input spectra comprise equally-weighted 5 & 12 keV components with equal abundance of 0.3 solar (A), 0.2 & 0.5 solar (B) and vice versa (C), respectively. Errors are the standard deviation of the 1000 Monte Carlo realisations in each case.

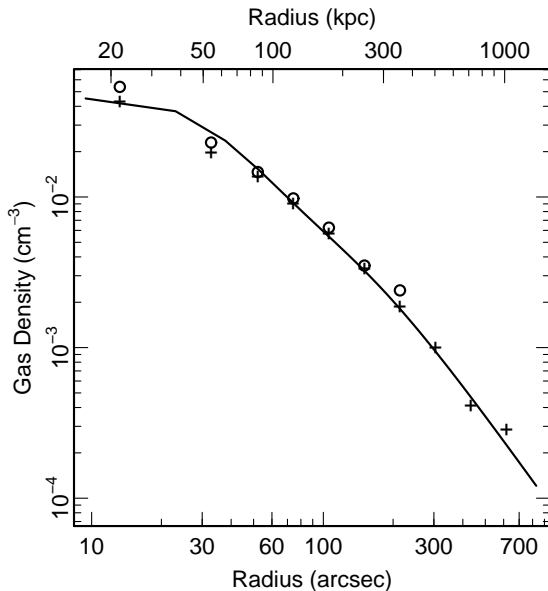


FIG. 5.— Gas electron number density as a function of radius. Errors on the density are too small to be plotted and the radial bin width error bars have been omitted for clarity. The hollow circles represent the *Chandra* points and the *XMM-Newton* data are the “+” symbols. Also shown is the *ROSAT* density profile from Mohr et al. (1999), plotted as a solid line for clarity.

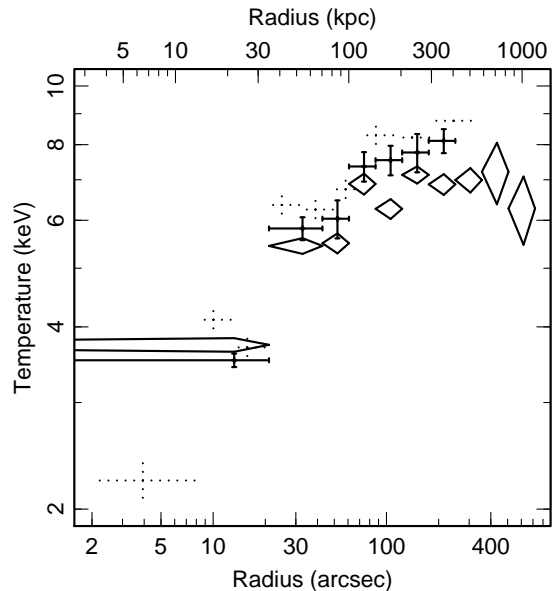


FIG. 6.— Deprojected temperature as a function of radius. The diamonds represent the *XMM-Newton* pn data and the barred crosses are the *Chandra* data. The dotted crosses are from the S03 analysis of the same *Chandra* observation, using older calibration data. Although some discrepancy between *Chandra* and *XMM-Newton* remains, it has been reduced with improvements to the CALDB and is less pronounced than in the projected $T(r)$ (Fig. 1).

originates. The best-fit normalization for each spectrum was converted directly into a mean gas density in the corresponding spherical shell, assuming a number density ratio given by

$$n_e = \frac{\mu_H}{\mu_e} n_H = 1.20 n_H, \quad (2)$$

appropriate for a fully ionized plasma with a metallicity of 0.3 times the solar value, using our adopted abundance table from Anders & Grevesse (1989).

Data from the outermost bin were discarded, since this volume incorporates a contribution from emission beyond the last shell that implies a non-trivial geometry for the purposes of determining the mean gas density. This leaves a total of 6 *Chandra* and 9 *XMM-Newton* radial bins, spanning the innermost 8.4' (835 kpc) of the ICM. Following Lewis, Buote, & Stocke (2003) we assign an effective radius to each annulus, which is approximately equivalent to an emission-weighted mean, given by (see McLaughlin 1999)

$$r = \left[0.5 \left(r_{\text{out}}^{3/2} + r_{\text{in}}^{3/2} \right) \right]^{2/3}. \quad (3)$$

The resulting density profile is plotted in Fig. 5, and also includes the data from the *ROSAT* analysis of Mohr et al. (1999), shown as the solid line. There is generally good agreement between the 3 sets of data, although the *Chandra* points appear to be systematically higher than *XMM-Newton*. It is particularly encouraging to note the close agreement between the *Chandra*/*XMM-Newton* values and the *ROSAT* profile, since the latter was derived from an analytical (double β -model with PSF corrections) fit, as compared to the non-parametric “onion peeling” method used in this analysis.

The corresponding deprojected gas temperature profile is shown in Fig. 6 with the *Chandra* and *XMM-Newton* points plotted as before. It can be seen that the *Chandra* temperatures are hotter, except for the innermost bin, where PSF scattering acts to smooth out the gradient in the *XMM-Newton* data. However, the agreement between the 2 observations is better than in the projected $kT(r)$, with an overlap in the 1σ error bounds for all but 3 annuli. The deprojected temperature gradient is steeper than that observed in the projected profile

(Fig. 1), as expected (since projection smooths out any such gradients), and reaches a minimum central value of ~ 3.5 keV. Also shown, for comparison, are the points from S03 using the same *Chandra* data, plotted as dotted crosses. These temperature values are systematically hotter than our measurements. We attribute this discrepancy to changes in the *Chandra* calibration between CALDB 2.15 and CALDB 2.26, particularly with respect to the method for handling the effects of the ACIS contamination, which causes an energy-dependent absorption that can affect temperature estimates. As can be seen, the newer ACIS calibration produces temperatures which are more consistent with those from *XMM-Newton*.

5. SPECTRAL MAPPING ANALYSIS

5.1. Hardness Method

Although the surface brightness of A478 appears to exhibit a smooth morphology typical of a relaxed cluster, it is difficult to gauge the true state of the gas from studying images alone. Here we describe the process of creating a temperature map from the *Chandra* X-ray data, based on a wavelet-smoothed hardness ratio image (Finoguenov et al. 2004b). The key advantage of this approach is that it allows fine scale temperature structure to be resolved, without any prior knowledge of its morphology, since we are able to work with high resolution images of the cluster.

We select two hardness bands, with the following energy ranges: 0.5–2.0 keV (soft band) and 2.0–7.0 keV (hard band). The hardness ratio (given by the hard band flux divided by the soft band flux) depends strongly on the gas temperature and the absorbing column along the line of sight, as well as more weakly on the metallicity of the gas. Under the assumption that the variation in absorbing column over the S3 chip is small (see the barred points in Fig. 3), we can therefore use the hardness ratio to estimate the temperature directly.

Taking the best-fit model to the global spectrum (§3), we fix the abundance and absorbing column and generate a series of 200 new models with different temperatures in the range 0.5–15.0 keV. For each of these spectra, we evaluate the ratio of the predicted model flux in the hard to soft bands. We then fit a 6th order polynomial curve to the data, to obtain an expression for the gas temperature as a function of hardness. The residuals from this best-fit relation are less than 1% throughout the range of hardness values to which we apply it.

To create a hardness ratio map from X-ray data it is necessary to apply some smoothing to suppress Poisson fluctuations. This ensures non-zero pixel values in the denominator (soft band image) but can also reveal subtle variations in hardness on small scales. We use a wavelet decomposition approach, which is ideal for highlighting low surface brightness diffuse emission, even in the presence of bright embedded point sources, whilst retaining complex structural information (see Vikhlinin et al. 1998, for details). This approach also provides information on the significance of structures identified on each scale and has recently been used in the analysis of *XMM-Newton* observations of several clusters (Finoguenov et al. 2004b,a; Henry, Finoguenov, & Briel 2004).

Initially we extract source and background images and corresponding exposure maps in both the soft and hard bands for the whole S3 chip. The corresponding background image is then subtracted from each hardness image, and the resulting image divided by the appropriate exposure map. The exposure maps are obtained by weighting the contributions to the effective area of the detector by the best-fitting model to the

global spectrum fitted in §3, within each of the soft and hard bands separately. Pixels with an equivalent exposure less than 25% of the highest value within the S3 chip were masked out to improve the S/N of the resulting hardness image.

A wavelet transform decomposition was then applied separately to the soft and hard band images, over 6 different scales sizes, increasing in integer powers of 2 from 2^2 pixels to 2^7 pixels, corresponding to angular sizes of $\sim 2''$ and $\sim 1'$, respectively. A 5σ threshold was used to identify genuine sources, whose extent was defined to enclose those neighboring pixels lying above a 2σ threshold. Following Finoguenov et al. (2004b), an additional smoothing was applied to each wavelet transform in turn, by convolving it with a Gaussian kernel of width equal to that scale, to reduce discontinuity artifacts associated with separating the image into different scales. The soft and hard band images were reconstructed by summing all six smoothed wavelet transformed images obtained at each of the scale sizes. The final hardness map was obtained as the ratio of the hard to soft images. Each pixel was then converted into a temperature value by using the polynomial relation derived above, with unphysical hardness values (confined to a few pixels near the S3 chip boundary) masked out of the resulting temperature map (i.e. values lying outside the fitting range of the calibration curve).

5.2. Spectral Fitting Method

There are several key assumptions of the hardness-based approach to generating a temperature map that could produce incorrect results. Specifically, there may be subtle, small-scale variations in absorbing column and gas metallicity that could manifest themselves as spurious features in the inferred temperature distribution. Here we present a more sophisticated method to determine spatial variations in gas temperature, in order to assess the validity of the above technique.

With an estimated temperature map we are well positioned to identify interesting features in the image for targeting with a conventional spectral fitting approach. Using contour maps of the temperature and soft band images, we defined a series of 53 separate regions, each containing a minimum of 1000 counts in the raw image, originating from gas of similar projected temperature and surface brightness, as implied by our wavelet decomposition analysis.

We extract source and background spectra and response files in each of these 53 regions, and fit each with an absorbed MEKAL model as before. Images of these regions, showing the best-fit temperature and 1σ bounds, are plotted in the lower half of Fig. 7. The color table for the spectral fit temperature map is identical to that used in the hardness temperature maps in the upper half of the figure. The broad features in the hardness map are confirmed in the spectral map: specifically, the temperatures of the cool core and surrounding regions agree very well. Moreover, the spectral analysis confirms the existence of 4 prominent hot spots located around the cluster center, with temperatures as high as 12 keV – almost double that of the surrounding medium in all cases, albeit with large uncertainties. The origin of these hot spots is unclear, but it seems unlikely that they can all be attributed to point source contamination: visual inspection of the raw image reveals no evidence for a surface brightness excess at these locations. We will return to the interpretation of these features in §6.1.

5.3. Spectral Mapping Deprojection

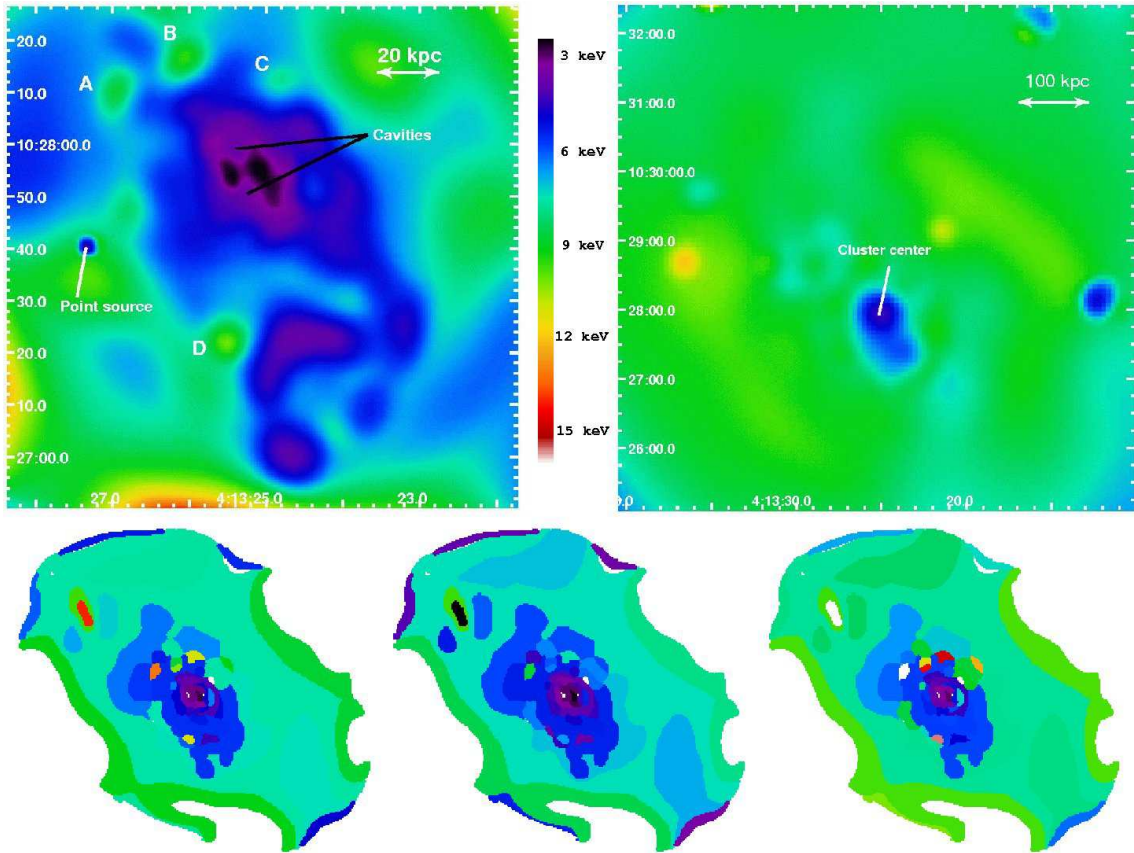


FIG. 7.— Wavelet smoothed temperature maps of A478 from *Chandra* (top left) and *XMM-Newton* (top right), derived from the hardness ratio method. The positions of 4 hot spot regions are indicated by the letters A-D, and the cavities discovered by S03 are also labeled. The bottom half shows the *Chandra* temperature map derived from the spectral fitting method; from left to right the panels show the best-fit values, 1σ low and upper limits on the temperature. The innermost green/yellow/orange regions are the hot spots.

Using our spectral mapping results, it is possible to perform an approximate deprojection, to provide a comparison with the “onion-peeling” method. To achieve this, we assume that all the emission projected onto each region originates in a spherical shell bounded by the inner- and outermost radii enclosing the region, measured from the surface brightness centroid used previously. The volume used to calculate the gas density from the MEKAL normalization (equation 1), is formed from the intersection of this shell with the cylinder having the cross section of that region. A more detailed description of this approach is presented in Henry et al. (2004).

In this “deprojection” scheme, no attempt is made to model out or otherwise remove the contaminating emission from regions outside of the volume element under consideration, which are projected onto the spectral region. Therefore, we take the projected temperature and metallicity information to apply to the 3-dimensional volume element. However, in selecting these regions, we have ensured that that gas is essentially isothermal as measured in projection, which minimizes the additional smoothing effect of averaging over a range of temperatures. Correspondingly the inferred temperatures and abundances are more likely to be representative of the deprojected gas properties.

A plot of the temperature profile from the mapping analysis is presented in Fig. 8, with the radial axis expressed in units of R_{500} (1349 kpc), as determined from our mass model of the cluster (see §5.4). It can be seen that there is a large degree of temperature scatter, with the hot spots clearly visible, al-

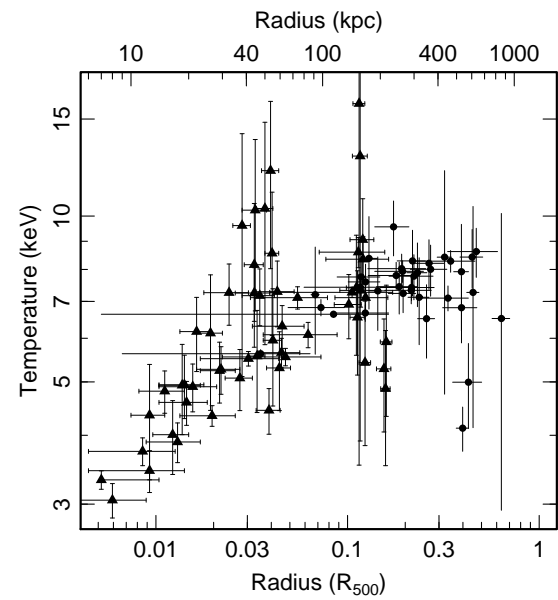


FIG. 8.— Temperature profile from the spectral mapping analysis. No discrepancy between the *Chandra* (diamonds) and *XMM-Newton* (solid circles) points is evident in the mapping data.

beit with large errors. The overlap between the *Chandra* and

XMM-Newton spectral mapping data is somewhat limited, due to the poorer spatial resolution of *XMM-Newton* combined with the impact of edge effects in the wavelet reconstruction limiting the outer radius of data from the *Chandra* S3 chip. However, it can be seen that the discrepancy between *Chandra* and *XMM-Newton* found in the annular spectral fits is not apparent in the spectral mapping data. Although this is due in part to the larger uncertainty in the data points, it may also point to the source of the discrepancy being the varied temperature structure in the ICM, which gives rise to a range of temperatures within a given annulus. Since *XMM-Newton* is more sensitive to cooler temperatures and *Chandra* is more sensitive to hotter ones, such a situation is likely to lead to a bias in fitting a single temperature spectrum, as observed. Moreover, the iron ionization fit is more sensitive to cooler gas phases, which emit proportionately more line flux, which explains why the *Chandra* 6.0–6.8 keV result (Table 2) was in good agreement with *XMM-Newton*.

Fig. 9 shows the entropy profile from the spectral mapping analysis. Also shown, as a dashed line, is a fit of the form $S \propto r^{1.1}$ (c.f. Tozzi, Scharf, & Norman 2000), which has been shown to provide a good match to the outer regions of most reasonably relaxed clusters (Ponman et al. 2003). To highlight the trend in the data, the points have been smoothed using a locally weighted regression in log-log space (solid line). This technique smooths the data using a quadratic function which is moved along the set of points to build up a curve, in an analogous fashion to how a moving average is computed for a time series. The algorithm used is implemented in the LOWESS function in the R Project statistical environment package⁴ (version 2.0.0) (R Development Core Team 2004), and further details can be found there. The agreement in the outer regions between this curve and the $S \propto r^{1.1}$ line is striking, although the data deviate slightly above this simple relation in the cool core (within $\sim 0.1 R_{500}$ – see Fig. 8). We defer further discussion of this issue to §6.3.

5.4. Mass Distribution

The deprojected gas $T(r)$ and $\rho(r)$ can be used to infer the gravitating mass profile, assuming hydrostatic equilibrium, given by

$$M_{\text{grav}}(r) = -\frac{kT(r)r}{G\mu m_p} \left[\frac{d\ln \rho}{d\ln r} + \frac{d\ln T}{d\ln r} \right], \quad (4)$$

(e.g. Fabricant, Lecar, & Gorenstein 1980), where μ is the mean molecular weight of the gas and m_p is the proton mass. In order to evaluate analytically the gradients in this equation, we fit a 3rd order polynomial to both the $T(r)$ and $\rho(r)$ data in log space. The resulting mass profile is evaluated at the radii of the input $T(r)$ and $\rho(r)$ values and is well described by a profile of the form

$$\rho(r) = \frac{\rho_0}{x^n (1+x)^{3-n}}, \quad (5)$$

(e.g. Zhao 1996), where ρ_0 is the central density, $x = r/r_s$, and r_s is a characteristic scale radius. For $r \ll r_s$ the profile is characterized by a cusp, with $\rho \propto r^{-n}$. Equation 5 is the generalized form of the so-called NFW profile (Navarro, Frenk, & White 1995), which is obtained for $n = 1$. A reasonable proxy for the virial radius of the halo can be obtained from r_{200} , the radius enclosing a mean overdensity of

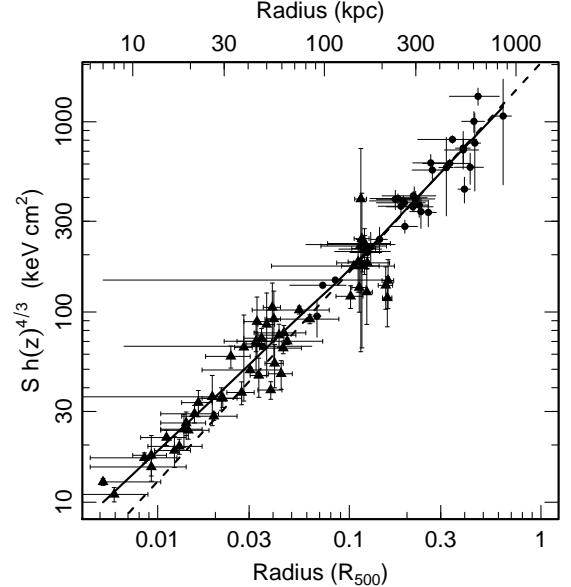


FIG. 9.— Entropy profile from the spectral mapping deprojection. The point styles are the same as in Fig. 8. The dashed line is an unweighted fit to the data, of the form $S \propto R^{1.1}$. For comparison, the solid line shows a locally weighted regression of the data in log-log space, using the method described in §6.1.

200 with respect to the critical density, $\rho_{\text{crit}}(z)$, of the Universe at the observed cluster redshift, z , given by

$$\rho_{\text{crit}}(z) = E(z)^2 \frac{3H_0^2}{8\pi G},$$

where G is the gravitational constant, H_0 is the Hubble constant at $z = 0$ and

$$E(z) = (1+z) \sqrt{1 + (z\Omega_m) + \frac{\Omega_\Lambda}{(1+z)^2} - \Omega_\Lambda},$$

equal to 1.042 for our adopted redshift and cosmology. The concentration of the NFW halo, c , is then obtained as r_{200}/r_s .

To provide better constraints on the mass distribution in the core of A478, we perform a finer binned “onion-peeling” analysis using just the *Chandra* data, which has much higher spatial resolution compared to *XMM-Newton*. The resulting gas density and temperature profiles are plotted in Figs. 10 & 11, together with the best-fit 3rd order polynomial curve (in log-log space) to the data. These smoothed curves were used to evaluate the logarithmic gradients needed to determine the mass profile using equation 4. Since we have fitted these polynomials in log-log space, the logarithmic gradient is simply the derivative of the function.

The cumulative mass distribution was calculated at the radius of the input $T(r)$ and $\rho(r)$ data, but using the values of the best-fit curve, rather than the measured data points. We have excluded the innermost bin since the gradient at this point is rather uncertain; we are more confident about the outermost bin since the turn-over implied by the best-fit curve is consistent with the temperature profile from *XMM-Newton*, which extends beyond this radius (see the diamonds in Fig. 6), and is also confirmed by the *Chandra* analysis of Vikhlinin et al. (2004), which extends beyond the S3 chip. The mass profile is plotted in Fig. 12, together with the best-fit mass function obtained with equation 5. The errors were determined from

⁴ <http://www.r-project.org>

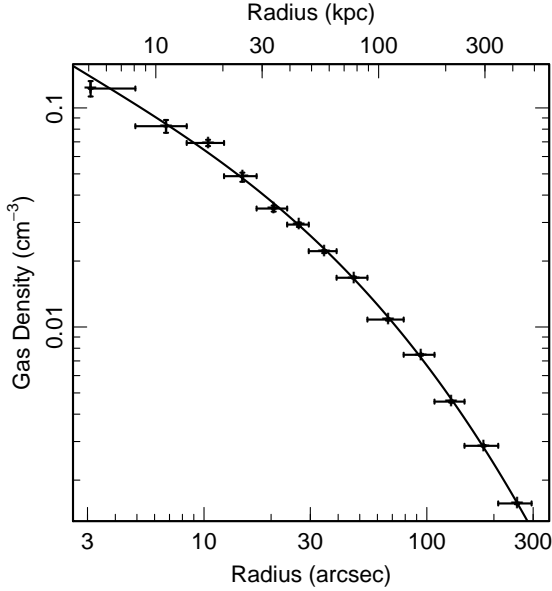


FIG. 10.— High-resolution *Chandra* gas density profile. The solid line is the best-fit 3rd order polynomial relation in log-log space.

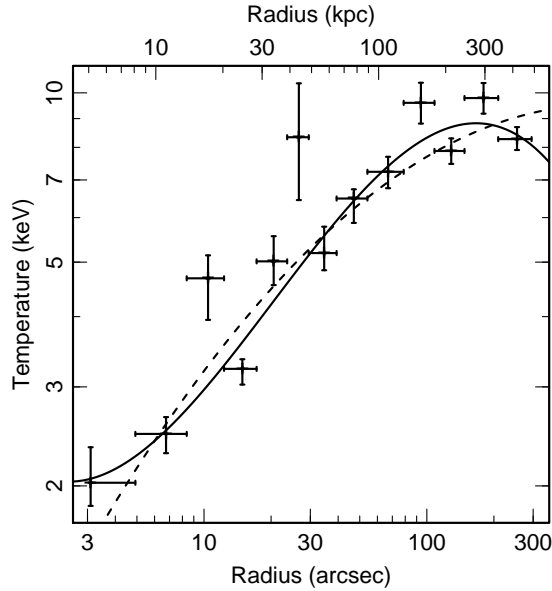


FIG. 11.— High-resolution *Chandra* gas temperature profile. The dashed and solid lines are the best-fit 2nd and 3rd order polynomial relations in log space, respectively.

a series of 2000 Monte Carlo realizations of the input $T(r)$ and $\rho(r)$ data; in each case a best-fit mass model (equation 5) was fitted and the errors on the model parameters were obtained from the standard deviation of the set of points. Also plotted is the gas fraction profile (Fig. 13), which actually *decreases* with radius out to ~ 200 kpc, beyond the confines of the central galaxy, somewhat contrary to expectation (e.g. David, Jones, & Forman 1995; Sanderson et al. 2003).

We find a best fit index parameter of $n = 0.35 \pm 0.22$, with a corresponding scale radius and concentration parameter of $r_s = 317 \pm 82$ kpc and $c = 6.9 \pm 1.6$, giving a value of $R_{200} = 2190 \pm 125$ kpc and $R_{2500} = 620 \pm 70$ kpc. Allen et al. (2003) and Schmidt, Allen, & Fabian (2004) also measured

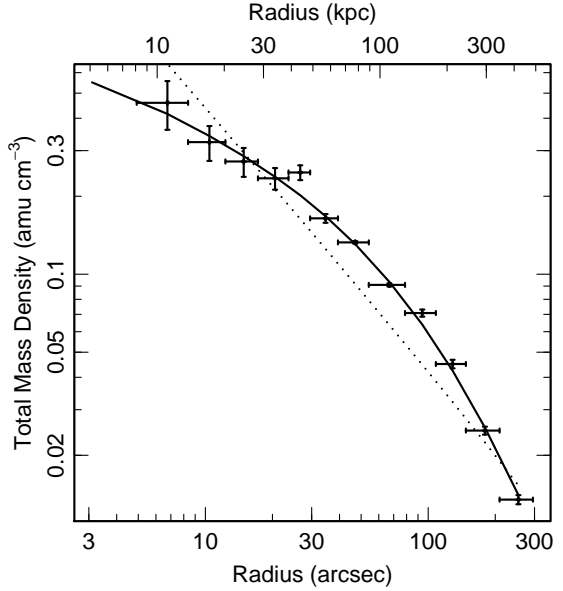


FIG. 12.— Mass profile from the *Chandra* data. The solid line is the best fit using Equation 5, with an inner logarithmic slope of -0.35 ± 0.22 ; for comparison, the dotted line shows the best-fit NFW profile (inner logarithmic slope of -1). The 1σ errors were generated from a set of 2000 Monte Carlo simulations.

the *Chandra* mass profile for A478, but fitted it with an NFW profile (i.e. n fixed at 1), to give $R_{200} = 2464^{+190}_{-120}$ kpc (converted to $H_0=70$) and $R_{200} = 2367$ kpc, respectively. Pointecouteau et al. (2004) also fitted an NFW profile to the poorer-resolution *XMM-Newton* data, to derive a value of $R_{200} = 2100 \pm 100$ kpc, in reasonable agreement with our findings. We estimate a total mass within R_{200} of $(1.3 \pm 0.27) \times 10^{15} M_\odot$, compared to $(1.84^{+0.48}_{-0.24}) M_\odot$ for Allen et al., and $(1.1 \times 10^{15}) M_\odot$ for Pointecouteau et al..

To investigate the robustness of our $M(r)$ inner logarithmic slope measurement, we have also computed the mass profile for the case where a 2nd order polynomial is fitted to the temperature points (the dashed line in Fig. 11). In this case we recover a slightly steeper index of $n = 0.49 \pm 0.24$. However, we note that a 2nd order polynomial indicates a rising $T(r)$ beyond the data points, whereas the 3rd order polynomial curve exhibits a turn-over that is clearly preferred by our *XMM-Newton* data, as well as the *Chandra* ACIS-I projected temperature profile of Vikhlinin et al. (2004). We return to discuss the mass distribution in §6.4.

6. DISCUSSION

6.1. Hot spots in the ICM

While there is generally a surprising amount of temperature structure present in the ICM in A478, of particular note are four “hot spots” seen in the inner regions of the core (see Fig. 7). Three of them are located to the North of the core; the other is to the South, and they all lie within ~ 30 –60 kpc of the center. There are no known cluster galaxies located at the position of these features, and they all lie just outside the edge of the central cluster galaxy, PGC014685: its d_{25} diameter (the isophote at which the optical B band surface brightness reaches 25 mag/arcsec 2) is 57 kpc (Paturel et al. 1997).

All four regions are clear outliers in both the temperature (Fig. 8) and pressure (Fig. 14) profiles, but occupy a relatively small volume. Correspondingly they produce an essentially

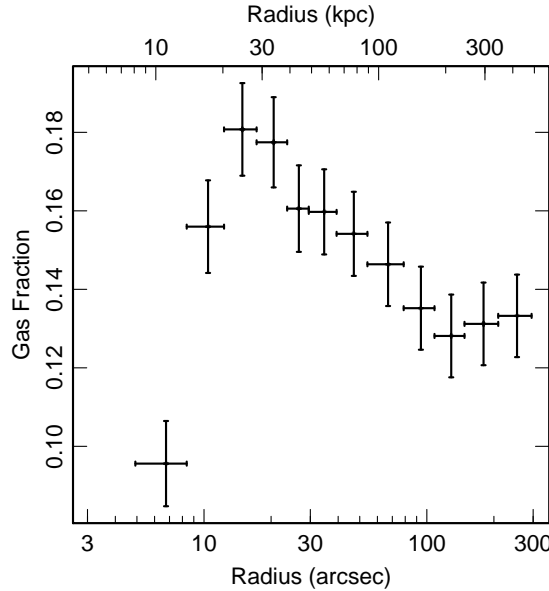


FIG. 13.— *Chandra* gas fraction profile, which shows an unusual decrease with radius within the cool core, beyond the central galaxy. The 1σ errors were generated from a set of 2000 Monte Carlo simulations.

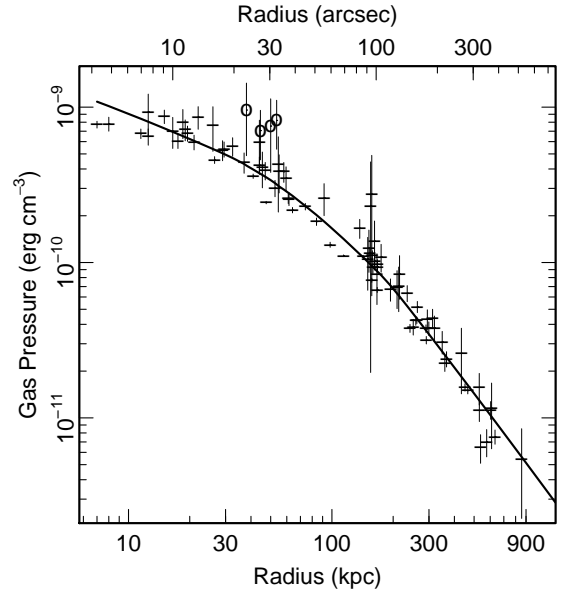


FIG. 14.— Pressure profile from the spectral mapping deprojection, with a smoothed curve shown as a solid line (see text for details). The hot spots are plotted as open circles. The X axis error bars have been omitted for clarity.

negligible distortion in the X-ray surface brightness distribution of the core of A478. The entropy of the hot spots also appears to be systematically higher than expected. Compared to the smoothed regression relation plotted in Fig. 9, there is an excess entropy of between 20–50 keV cm 2 present in each of the hot spots, corresponding to 30–50% of the expected value. The combination of excess pressure and entropy indicates that these are strong shocks, and therefore unlikely to be the result of sound waves or mildly supersonic motion. However, the volume enclosing the hot spots is too small for them to produce a noticeable surface brightness contrast compared to the bright emission from the cool core.

Some key properties of these hot spots are summarized in Table 4, including the estimated excess thermal energy present in each one, based on the excess gas pressure and estimated volume. This excess was measured relative to an estimate of the underlying $P(r)$, obtained from a locally weighted regression of the data in log-log space (the solid curve in Fig. 14), using the method described in §5.3. The excess energy in each hot spot was calculated by multiplying its residual excess pressure above this curve by the estimated volume for the region. Although the errors on the individual estimates are quite large, the total excess thermal energy contained in all 4 hot spots combined is $(3 \pm 1) \times 10^{59}$ ergs. We note that this result depends only weakly on the volume, V , assumed for the hot spots: the energy, $E \propto V\rho$, and $\rho \propto \sqrt{K/V}$ (Equation 1), where K is the MEKAL model normalization, which implies $E \propto \sqrt{KV}$.

The global morphology of A478 exhibits a regular structure, and the *XMM-Newton* hardness temperature map (top right panel of Fig. 7) shows no sign of significant disturbance in the outskirts of the ICM. This, combined with the presence of a well established cool core, suggests that A478 cannot have experienced a recent merger or significant disturbance, which might account for the existence of the hot spots. It can be seen from Table 4 that the distances from the cluster center and energy excesses are similar for all the hot spots. Further-

more, they appear to be located (see top left panel of Fig. 7) in rough alignment with the (approximately) conical depressions discovered by S03, corresponding to radio lobes emitted from the active nucleus in the central galaxy. These characteristics point to the influence of an event originating in the cluster center. Correspondingly, it is reasonable to associate them with AGN activity.

On the basis that the hot spots share a common origin, we have extracted a combined spectrum from all 4 regions and fitted it with a single absorbed MEKAL model. In this way we can gain a better understanding of the degree to which the gas has been heated. We obtain a best fit temperature of $12.1_{-2.6}^{+3.4}$ keV; an abundance of $0.26_{-0.26}^{+0.40}$ solar and absorption of $(2.4_{-0.2}^{+0.3} \times 10^{21})$ cm $^{-2}$. However, by fixing the temperature to the ambient value of 5.5 keV (e.g. see the best-fit curve at ~ 50 kpc in Fig. 11) and refitting with the other parameters left free to vary, we obtain a change in fit statistic of $\Delta\chi^2 = 16.7$, corresponding to 4.1σ significance.

We stress that the interpretation of this result as evidence for the existence of the hot spots hinges on the validity of associating these 4 separate regions with each other. It is certainly possible to achieve a similar level of significance by randomly grouping hot regions arising from purely statistical fluctuations. However, we believe that the location of the hot spots in the cluster core points to an association between them that indicates they are not merely random peaks in the temperature distribution. Specifically, they lie within a narrow annulus centered on the cluster peak, and they are positioned within the range of angles that enclose the roughly conical bipolar cavities excavated by radio lobes from the central AGN.

6.2. AGN Heating?

If the hot spots are indeed the result of AGN activity, we can address the issue of how they may be connected to the cavities seen in the ICM. The fact that the hot spots are located at least 3–4 times further away from the cluster center implies a different formation mechanism to that which excavated the

TABLE 4
DATA FOR THE HOT SPOTS IN THE CENTRAL ICM OF A478

Region	Distance ^a (kpc)	Cts ^b	kT (keV)	χ^2/dof	L_X^c (10^{42} erg/s)	Vol ^d (10^{68} cm 3)	ΔE^e (10^{58} erg)	t_{cool}^f (yr)
A	48–59	1054	$12.1^{+2.6}_{-5.0}$	57.65/43	9.3	2.3	11 ± 6	6×10^8
B	34–42	727	$9.6^{+2.5}_{-4.4}$	28.93/29	6.7	0.9	4.6 ± 4	4×10^8
C	38–51	1108	$10.3^{+2.7}_{-3.6}$	45.08/45	10	2.6	8.7 ± 6.5	6×10^8
D	45–55	639	$10.3^{+3.2}_{-4.5}$	25.99/25	5.4	1.2	5.0 ± 4.6	5×10^8

NOTE. — ^aNearest/furthest distance to hotspot, measured from the cluster center; ^bnet source counts in the 0.5–7.0 keV band; ^cbolometric X-ray luminosity; ^destimated volume of region; ^eestimated excess energy in hot spot; ^fgas cooling time (E/L_X , using the *total* rather than the excess hot spot energy). All errors are 1σ .

cavities. In addition, S03 estimate that the minimum energy needed to create these cavities is $\sim 3 \times 10^{58}$ ergs (Bîrzan et al. 2004) estimate $\sim 1.2 \times 10^{58}$ ergs), which is a tenth of the thermal energy contained in the hot spots. S03 further estimate a cavity age of $\sim 3 \times 10^7$ yr, from the time taken for the bubbles which formed them to rise buoyantly to their observed location. Similarly, Bîrzan et al. estimate a cavity age of between $1–3 \times 10^7$ yr, by considering 3 different timescales. For comparison, the time taken to reach a distance of 50 kpc at the local sound speed (920 km s $^{-1}$) is $\sim 5 \times 10^7$ yr, for a mean ambient gas temperature of 5 keV ($c_s = 1480(T_g/10^8 \text{ K})^{1/2}$ km s $^{-1}$ (Sarazin 1988)). There is no evidence of a bow shock or X-ray emission excess anywhere near these features, which argues against very recent supersonic motion. It is more likely that the hot spots may have been generated *in situ*, perhaps in a similar manner to radio hot spots located at the shock termination of radio jets, which have been observed at similar distances from the cluster center (e.g. see the recent sample of Hardcastle & Sakelliou 2004).

An estimate of the minimum time scale for heat conduction to erase the hot spots can be obtained by considering the saturated heat flux, given by

$$q_{\text{sat}} = 0.4 \left(\frac{2kT_e}{\pi m_e} \right)^{1/2} n_e k T_e \quad (6)$$

(Cowie & McKee 1977), where m_e is the electron mass. For hotspot A the gas density is 2×10^{-4} cm 3 and its temperature is 12 keV. Assuming a spherical geometry for this region, with a volume of 2.3×10^{68} cm 3 (Table 4), yields a cooling rate of 10^{44} erg s $^{-1}$. Thus, it would take $\sim 3 \times 10^7$ yr to lose its excess energy, of 10^{59} erg, via conduction. This is about a tenth of the likely lifetime of the hot spots, which implies that heat conduction must be suppressed by a factor of ~ 10 compared to the Spitzer rate. Such a decrease in conduction efficiency could easily be achieved by magnetic fields, which have been shown to lead to suppression factors of ~ 5 in a weakly collisional magnetized plasma (Narayan & Medvedev 2001).

The positions of the Northern set of 3 hot spots (Fig. 7) may offer a clue as to the mechanism responsible for their creation. Their spacing is suggestive of a wide jet opening angle, of roughly 100 degrees. This is consistent with the slow jet heating scenario of Soker & Pizzolato (2004), which relies on such a wide angle to produce a poorly collimated, massive and relatively slow outflow. Moreover, the emissivity of the small bubbles in the ICM predicted from this model is too low for them to be detected in X-ray images with existing telescopes, consistent with the hot spots in A478. The Soker & Pizzolato model is similar to the effervescent heating model of Begelman (2001), which also postulates the forma-

tion of many small bubbles, which heat the ICM by doing PdV work as they expand and rise. A particularly attractive aspect of this scenario is that the heating is smoothly regulated, since gas cooling acts to steepen the ICM pressure profile, thus yielding more energy from the bubbles' expansion so as to balance the cooling. However, this mechanism for heating the ICM would need to be slow enough to avoid disrupting the nearly power-law scaling of entropy with radius seen in Fig. 9.

While the interaction of AGN with the intracluster medium has been well studied in recent simulations (e.g. Rizza et al. 2000; Reynolds, Heinz, & Begelman 2001; Churazov et al. 2001; Brüggen & Kaiser 2002; Basson & Alexander 2003; Ruszkowski et al. 2004a), the formation of shock heated blobs of the type seen in A478 does not appear to be a generic feature. However, Clarke, Harris, & Carilli (1997) present 3D magnetohydrodynamical simulations of a supersonic jet, which predict the formation of a pair of X-ray excesses, correspondingly to shocked ambient gas, at either side of the jet orifice, which itself produces an X-ray cavity of the type seen in A478. The Clarke et al. simulations proceed for $\sim 10^7$ yr, which does not allow enough time to track the full evolution of these excesses. However, it seems probable that the shock heated gas in these blobs would expand outwards and heat the ICM, which could be an important means of transferring AGN mechanical luminosity into gas thermal energy.

Similarly, the more recent simulations of Omma et al. (2004) appear to produce three distinct density enhancements surrounding the head of an AGN outflow, appearing after $\sim 10^8$ yr. However, the jet responsible for these features is only weakly relativistic, so may not be capable of heating these blobs at the level observed in A478. Observationally, perhaps the closest analogue to the hot spots reported here is the heated bubble observed in MKW 3s by Mazzotta et al. (2002). This feature lies at roughly 90 kpc from the cluster core and is approximately 25 kpc in radius in the plane of the sky. More recently, Mazzotta et al. (2004) present new, lower frequency radio observations for this cluster, which show that the radio emission is fully enclosed by the shocked gas. A similar radio/X-ray interaction is observed in Hydra A, where expanding radio lobes, observed at 330 MHz, appear to be driving a shock front (Nulsen et al. 2004). It is possible that equivalent lower frequency observations of A478 may reveal larger radio lobes than those seen in the 1.4 GHz VLA map (shown in Sun et al. 2003), which might show some evidence of an interaction with the hotspot regions.

However, unlike A478, the MKW 3S bubble is clearly visible as a depression in the surface brightness and the Hydra A shock front is revealed as a discontinuity in the X-ray im-

age. Similarly, there are spiral arm-like features observed by *Chandra* in the elliptical galaxy NGC 4636, produced by weak shocks driven by off center outbursts (Jones et al. 2002). However, these are ostensibly density enhancements, which produce a clear signature in the surface brightness – as already noted, the hot spots seen in A478 are effectively invisible in X-ray images.

There is further evidence of possible AGN activity disturbing the gas in the form of a tentative “ripple” in the surface brightness profile of the core (Fig. 15). We have generated an unsharp mask image, using the method of Ruszkowski et al. (2004b), who have simulated viscous dissipation in the ICM caused by AGN activity. A 0.5–7.0 keV raw image was smoothed with a Gaussian kernel of FWHM 6 kpc ($\sigma=3.1$ pixels) and subtracted from the unsmoothed image; the resulting image has been smoothed with a Gaussian kernel of $\sigma = 1.5$ pixels to highlight the features present. The depressions caused by the radio lobes are clearly seen, producing an “H” shape which resembles that seen in the Ruszkowski et al. (2004b) simulations, and there is also a suggestion of a “ripple” to the North of the center, lying between 16 and 26 kpc of the AGN. This ripple has a low contrast, but is clearly longer and more coherent than the typical noise features in the image. It is reminiscent of the ripples seen in the ICM of the Perseus (Fabian et al. 2003) and Virgo (at 14 and 17 kpc) (Forman et al. 2004) clusters, which are attributed to shock fronts emanating from the AGN in the central cluster galaxy. If this ripple is genuine, the implied travel time for the feature is roughly 2×10^7 yr (given the assumed local sound speed of 920 km s^{-1} used above), which is comparable to the age of the cavities. We note that the hot spots in A478 are not visible in the unsharp mask image and that they lie at least twice as far out as the putative ripple.

6.3. Entropy Profile

The radial variation in gas entropy in A478 (Fig. 9) is unusual, in that it appears to follow a broken power law relation, with an outer logarithmic slope of ~ 1.1 and a slightly shallower inner slope of ~ 0.95 within $\sim 0.1 R_{500}$, but with no indication of a flattening in the core. Non cool-core clusters generally exhibit a flattening of the entropy profile towards the center (e.g. Rasmussen & Ponman 2004; Pratt & Arnaud 2005), while the effect of cooling is to lower the entropy in exactly this region. It therefore appears to be a conspiracy that causes these two effects to counterbalance each other so as to preserve the scaling evident in the outskirts, where cooling is insignificant. A recent *XMM-Newton* study of 13 nearby cool core clusters has found that their entropy profiles follow a power-law with best-fit logarithmic slope of 0.95, out to roughly half the virial radius (Piffaretti et al. 2005). However, other cool core clusters show evidence of flattening in their core entropy profile (e.g. Pratt & Arnaud 2003; O’Sullivan et al. 2003; Wise et al. 2004). Moreover, the slope of ~ 1.1 is predicted to arise from shock heating due to accretion of gas (Tozzi et al. 2000; Tozzi & Norman 2001), which would not be expected to persist in cooling-dominated cluster cores.

The shape of A478’s entropy profile resembles that of the fossil group NGC 6482 ($kT \sim 0.7$ keV), which was the subject of a recent *Chandra* analysis (Khosroshahi et al. 2004). That observation is restricted to the inner 10% of R_{200} of the halo, but it is clear that the entropy data are consistent with a power law form, with a logarithmic slope slightly shallower than $S \propto r^{1.1}$. Since NGC 6482 is a fossil group, it is expected

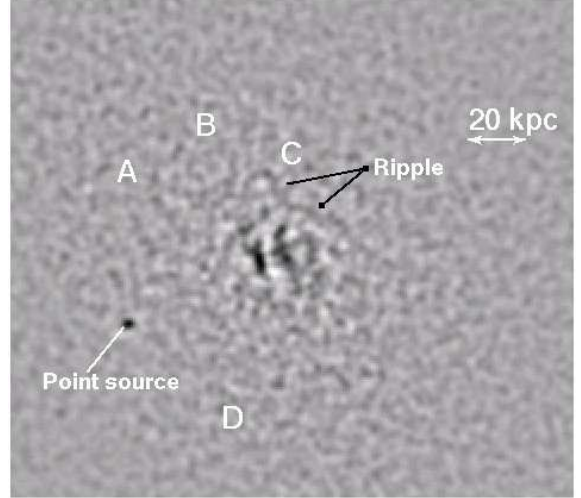


FIG. 15.— An unsharp masked 0.5–7.0 keV *Chandra* image of the core of A478. Each pixel is $0.492''$ (0.8 kpc) across and the image has been smoothed with a Gaussian of $\sigma = 1.5$ pixels. The edges around the radio lobe cavities are clearly visible as an “H” shape, and there is evidence of a possible curved “ripple” to the North of the cavities. The positions of the other features are labeled exactly as positioned in Fig. 7.

to be a very old system. However, it shows no evidence for strong cooling and, furthermore, has a gas temperature profile which decreases monotonically with radius, thus ruling out thermal conduction as a means of heating the core. Since NGC 6482 shows some evidence of having a mildly active nucleus, it is possible that this system too has been subjected to a phase of AGN heating which has only recently abated, where significant gas cooling is presently being reestablished.

Given the apparently significant impact of the AGN on the gas in the core of A478, it is worth noting that excessively large heat input would trigger convective motions that would stir up the gas, flattening the entropy profile and erasing abundance gradients in the core (Churazov et al. 2001; Brüggen 2002; Churazov et al. 2002). As there is some enhancement in the metallicity towards the center the ICM (Fig. 2), it is unlikely that a significant disturbance could have occurred recently. This may be because the AGN heating is widely distributed (e.g. effervescent) and thus not very vigorous. Alternatively, it could indicate that the most unstable (i.e. lowest entropy) gas is also the most metal rich, and that as it cools and moves inwards it produces a central abundance peak.

The cooling time of gas in the center of A478 is only $\sim 9 \times 10^7$ yr — roughly 6 times shorter than the cooling time of the hot spots (see Table 4). S03 point out that the observed radio lobes are much smaller than the X-ray cavities, which suggests a fading of the radio source on a timescale of $\sim 10^{7-8}$ yr. Furthermore, the ratio of mechanical power needed to excavate the cavities to the current radio power of the AGN is over 1000 (Bîrzan et al. 2004) — by far the largest ratio amongst the 10 clusters (from their sample of 18 objects) for which they have such data. The inclusion of the hot spot contribution to the energy budget raises this value even higher. Therefore, it is possible that we are witnessing the rapid reestablishment of a cluster cooling flow, following a period of AGN heating of the gas, before the cavities have been completely refilled. On the other hand, an AGN can vary in radio power while its jet power remains constant (Eilek 2004; Bîrzan et al. 2004), and thus some mechanical heating of the ICM may be ongoing,

despite the fading radio luminosity, as possibly indicated by the putative “ripple” seen in Fig. 15.

If similar hot spot features are present in other clusters with radio lobe cavities, the timescale for which these features persist as over-dense blobs is short enough to make them unlikely to be detected in X-ray images. Furthermore, for much of this time they would reside in close proximity to the cluster center, where emission from the cluster core would be substantial, greatly reducing their surface brightness contrast. The alternative method of detecting them – locating the hot spots from their temperature signature – is also challenging, since it requires high resolution hardness mapping and the best possible data quality (the A478 *Chandra* observation analysed in this work comprises $\sim 400,000$ net source counts from the S3 chip).

6.4. Mass Profile

The soft core in the mass profile (Fig. 12) of A478 is unusual, and apparently at odds with numerical simulations of clusters, which indicate inner logarithmic slopes of -1 (Navarro et al. 1995) or even as steep as -1.5 (Moore et al. 1998). However, such a flat slope is permitted by purely analytical considerations of the dark matter, based on fundamental statistical mechanics: Hansen et al. (2005) have recently demonstrated that this approach permits $0 < n < 10/3$, for the index parameter in equation 5. Furthermore, a number of clusters have been found with similarly flatter cusps in their mass profiles. Tyson, Kochanski, & dell’Antonio (1998) measured a slope of 0.57 ± 0.02 , and Sand, Treu, & Ellis (2002) observed a value of 0.35 for two different clusters, based on strong gravitational lensing analyses. More recently, Sand et al. (2004) have studied lensing arcs in 6 clusters and report a mean slope of 0.52 ± 0.05 . It is interesting to note that their sample comprises only clusters with a dominant brightest cluster galaxy (BCG), as is the case for A478. Also, the cluster Abell 1795 has been shown to have an inner mass profile logarithmic slope of $0.59_{-0.17}^{+0.12}$ (90% confidence), inferred from a *Chandra* analysis (Ettori et al. 2002).

It must be remembered that, unlike lensing measurements, our X-ray analysis hinges on the assumption of hydrostatic equilibrium, which could easily break down in the core, given the impact of the central AGN. For example, the presence of significant non-thermal pressure support could mimic a less concentrated mass distribution. The simulations of Faltenbacher et al. (2005) indicate that random bulk motions of gas account for 10% of the total pressure support in clusters. Also, a recent *XMM-Newton* analysis of the spectrum of pressure fluctuations in the Coma Cluster found a lower limit of $\sim 10\%$ for the contribution to the ICM pressure support arising from turbulence. It is possible that bulk or turbulent motion of gas associated with AGN activity could be significant in the core of A478. Presumably such a mechanism would give rise to a radially diminishing pressure contribution, which could act to flatten the inferred mass distribution in the manner observed. In such a situation, the inferred gas fraction would be increasingly overestimated at smaller radii, which may explain the radially decreasing trend ob-

served within ~ 200 kpc in Fig. 13.

7. CONCLUSIONS

We have studied the detailed thermodynamic properties of the intracluster medium in the relaxed, cool-core cluster Abell 478, using *Chandra* and *XMM-Newton* X-ray data. Our main findings can be summarized as follows:

1. We find that our *Chandra* X-ray temperature measurements are systematically hotter than those from *XMM-Newton*, as also reported by Pointecouteau et al. (2004). By selecting approximately isothermal regions, we find slightly better agreement between the two. However, by simulating multiphase spectra and fitting them with a single temperature model, we find no evidence for significant disagreement between *Chandra* and *XMM-Newton*. We therefore conclude that the observed discrepancy cannot be fully attributed to non-isothermality in fitting single-temperature models.
2. The entropy profile appears to agree well with the empirical modified entropy scaling of Ponman et al. (2003). Moreover, the power law trend continues to the innermost radius measured (< 10 kpc), with only a slightly shallower slope. There is no evidence of any core in the entropy profile.
3. Under the assumption of hydrostatic equilibrium, we infer a mass profile that exhibits a soft core, characterized by a logarithmic slope of -0.35 ± 0.22 . This is significantly flatter than an NFW profile (slope = -1), but is consistent with the recent gravitational lensing results of Sand et al. (2004) for clusters containing a dominant central galaxy.
4. We have discovered four hot spots in the ICM located well within the cool core, where the gas is roughly twice as hot as its surroundings. The combined excess energy associated with these regions is $(3 \pm 1) \times 10^{59}$ erg, which is ~ 10 times the energy needed to excavate the cavities produced by radio lobes from the central AGN. The properties of these hot spots suggest they may be the result of strong shock heating from a jet/outflow originating in the AGN.

We are grateful to M. Arnaud and E. Pointecouteau for useful discussion and providing the results of their *XMM-Newton* analysis prior to publication. AS thanks Yen-Ting Lin for useful discussions, Ming Sun for providing his published *Chandra* profile data in electronic form, Ben Maughan for spotting a mistake in Equation 1 and the referee for helpful comments; AF thanks The University of Illinois for hospitality during his visit. This work is supported by NASA Long Term Space Astrophysics award NAG5-11415. This work has made use of the NASA/IPAC Extragalactic Database (NED) and the HyperLeda galaxy database.

REFERENCES

Afshordi, N., Lin, Y., & Sanderson, A. J. R. 2005, ApJ, accepted (astro-ph/0408560)
 Allen, S. W., Schmidt, R. W., Fabian, A. C., & Ebeling, H. 2003, MNRAS, 342, 287
 Anders, E. & Grevesse, N. 1989, Geochim. Cosmochim. Acta, 53, 197
 Arnaud, M. & Evrard, A. E. 1999, MNRAS, 305, 631
 Bîrzan, L., Rafferty, D. A., McNamara, B. R., Wise, M. W., & Nulsen, P. E. J. 2004, ApJ, 607, 800
 Basson, J. F. & Alexander, P. 2003, MNRAS, 339, 353

Begelman, M. C. 2001, in ASP Conf. Ser. 240: Gas and Galaxy Evolution, p.363, 363

Böhringer, H., Matsushita, K., Churazov, E., Ikebe, Y., & Chen, Y. 2002, *A&A*, 382, 804

Brüggen, M. & Kaiser, C. R. 2002, *Nature*, 418, 301

Brüggen, M. 2002, *ApJ*, 571, L13

Burns, J. O. 1990, *AJ*, 99, 14

Churazov, E., Brüggen, M., Kaiser, C. R., Böhringer, H., & Forman, W. 2001, *ApJ*, 554, 261

Churazov, E., Sunyaev, R., Forman, W., & Böhringer, H. 2002, *MNRAS*, 332, 729

Clarke, D. A., Harris, D. E., & Carilli, C. L. 1997, *MNRAS*, 284, 981

Cowie, L. L. & McKee, C. F. 1977, *ApJ*, 211, 135

Croston, J. H., Hardcastle, M. J., & Birkinshaw, M. 2005, *MNRAS*, 357, 279

David, L. P., Jones, C., & Forman, W. 1995, *ApJ*, 445, 578

de Plaa, J., Kaastra, J. S., Tamura, T., Pointecouteau, E., Mendez, M., & Peterson, J. R. 2004, *A&A*, 423, 49

Dickey, J. M. & Lockman, F. J. 1990, *ARA&A*, 28, 215

Edge, A. C. & Stewart, G. C. 1991, *MNRAS*, 252, 414

Eilek, J. A. 2004, in The Riddle of Cooling Flows in Galaxies and Clusters of galaxies (astro-ph/0310011)

Ettori, S., Fabian, A. C., Allen, S. W., & Johnstone, R. M. 2002, *MNRAS*, 331, 635

Fabian, A. C., Sanders, J. S., Allen, S. W., Crawford, C. S., Iwasawa, K., Johnstone, R. M., Schmidt, R. W., & Taylor, G. B. 2003, *MNRAS*, 344, L43

Fabian, A. C., Sanders, J. S., Ettori, S., Taylor, G. B., Allen, S. W., Crawford, C. S., Iwasawa, K., Johnstone, R. M., & Ogle, P. M. 2000, *MNRAS*, 318, L65

Fabricant, D., Lecar, M., & Gorenstein, P. 1980, *ApJ*, 241, 552

Fairley, B. W., Jones, L. R., Scharf, C., Ebeling, H., Perlman, E., Horner, D., Wegner, G., & Malkan, M. 2000, *MNRAS*, 315, 669

Faltenbacher, A., Kravtsov, A. V., Nagai, D., & Gottlöber, S. 2005, *MNRAS*, 358, 139

Finoguenov, A., Henriksen, M. J., Briel, U. G., de Plaa, J., & Kaastra, J. S. 2004a, *ApJ*, 611, 811

Finoguenov, A., Pietsch, W., Aschenbach, B., & Miniati, F. 2004b, *A&A*, 415, 415

Forman, W., Nulsen, P., Heinz, S., Owen, F., Eilek, J., Vikhlinin, A., Markevitch, M., Kraft, R., Churazov, E., & Jones, C. 2004, *ApJ*, submitted (astro-ph/0312576)

Fujita, Y., Suzuki, T. K., & Wada, K. 2004, *ApJ*, 600, 650

Gardini, A. & Ricker, P. M. 2004, *Mod. Phys. Lett.*, A19, 2317

Garilli, B., Bottini, D., Maccagni, D., Carrasco, L., & Recillas, E. 1996, *ApJS*, 105, 191

Hansen, S. H., Egli, D., Hollenstein, L., & Salzmann, C. 2005, *New Astronomy*, 10, 379

Hardcastle, M. J. & Sakelliou, I. 2004, *MNRAS*, 349, 560

Henry, J. P., Finoguenov, A., & Briel, U. G. 2004, *ApJ*, 615, 181

Jones, C., Forman, W., Vikhlinin, A., Markevitch, M., David, L., Warmflash, A., Murray, S., & Nulsen, P. E. J. 2002, *ApJ*, 567, L115

Kaastra, J. S., Tamura, T., Peterson, J. R., Bleeker, J. A. M., Ferrigno, C., Kahn, S. M., Paerels, F. B. S., Piffaretti, R., Branduardi-Raymont, G., & Böhringer, H. 2004, *A&A*, 413, 415

Khosroshahi, H. G., Jones, L. R., & Ponman, T. J. 2004, *MNRAS*, 349, 1240

Kim, W. & Narayan, R. 2003, *ApJ*, 596, 889

Lewis, A. D., Buote, D. A., & Stocke, J. T. 2003, *ApJ*, 586, 135

Lockman, F. J. 2004, in Soft X-ray Emission from Clusters of Galaxies and Related Phenomena (astro-ph/0311386)

Lumb, D. H., Finoguenov, A., Saxton, R., Aschenbach, B., Gondoin, P., Kirsch, M., & Stewart, I. M. 2003, in X-Ray and Gamma-Ray Telescopes and Instruments for Astronomy. Edited by Joachim E. Truemper, Harvey D. Tananbaum. Proceedings of the SPIE, Volume 4851 (2003), 255–263

Makishima, K., Ezawa, H., Fukuzawa, Y., Honda, H., Ikebe, Y., Kamae, T., Kikuchi, K., Matsushita, K., Nakazawa, K., Ohashi, T., Takahashi, T., Tamura, T., & Xu, H. 2001, *PASJ*, 53, 401

Mazzotta, P., Brunetti, G., Giacintucci, S., Venturi, T., & Bardelli, S. 2004, *Journal of Korean Astronomical Society*, 37, 381

Mazzotta, P., Kaastra, J. S., Paerels, F. B., Ferrigno, C., Colafrancesco, S., Mewe, R., & Forman, W. R. 2002, *ApJ*, 567, L37

McLaughlin, D. E. 1999, *AJ*, 117, 2398

McNamara, B. R., Wise, M. W., Nulsen, P. E. J., David, L. P., Carilli, C. L., Sarazin, C. L., O'Dea, C. P., Houck, J., Donahue, M., Baum, S., Voit, M., O'Connell, R. W., & Koekemoer, A. 2001, *ApJ*, 562, L149

Mohr, J. J. & Evrard, A. E. 1997, *ApJ*, 491, 38

Mohr, J. J., Matheson, B., & Evrard, A. E. 1999, *ApJ*, 517, 627

Moore, B., Governato, F., Quinn, T., Stadel, J., & Lake, G. 1998, *ApJ*, 499, L5

Narayan, R. & Medvedev, M. V. 2001, *ApJ*, 562, L129

Navarro, J. F., Frenk, C. S., & White, S. D. M. 1995, *MNRAS*, 275, 720

Nulsen, P. E. J., McNamara, B. R., Wise, M. W., & David, L. P. 2004, *ApJ*, submitted (astro-ph/0408315)

Omrao, H., Binney, J., Bryan, G., & Slyz, A. 2004, *MNRAS*, 348, 1105

Osmond, J. P. F. & Ponman, T. J. 2004, *MNRAS*, 350, 1511

O'Sullivan, E., Vrtilek, J. M., Read, A. M., David, L. P., & Ponman, T. J. 2003, *MNRAS*, 346, 525

Paturel, G., Andernach, H., Bottinelli, L., di Nella, H., Durand, N., Garnier, R., Gouguenheim, L., Lanoix, P., Marthinet, M. C., Petit, C., Rousseau, J., Theureau, G., & Vauglin, I. 1997, *A&AS*, 124, 109

Peterson, J. R., Kahn, S. M., Paerels, F. B. S., Kaastra, J. S., Tamura, T., Bleeker, J. A. M., Ferrigno, C., & Jernigan, J. G. 2003, *ApJ*, 590, 207

Piffaretti, R., Jetzer, P., Kaastra, J. S., & Tamura, T. 2005, *A&A*, 433, 101

Pointecouteau, E., Arnaud, M., Kaastra, J., & de Plaa, J. 2004, *A&A*, 423, 33

Ponman, T. J., Cannon, D. B., & Navarro, J. F. 1999, *Nature*, 397, 135

Ponman, T. J., Sanderson, A. J. R., & Finoguenov, A. 2003, *MNRAS*, 343, 331

Pratt, G. W. & Arnaud, M. 2003, *A&A*, 408, 1

—. 2005, *A&A*, 429, 791

R Development Core Team. 2004, R: A language and environment for statistical computing, R Foundation for Statistical Computing, Vienna, Austria, ISBN 3-900051-00-3

Rasmussen, J. & Ponman, T. J. 2004, *MNRAS*, 349, 722

Reynolds, C. S., Heinz, S., & Begelman, M. C. 2001, *ApJ*, 549, L179

Rizza, E., Loken, C., Bliton, M., Roettiger, K., Burns, J. O., & Owen, F. N. 2000, *AJ*, 119, 21

Ruszkowski, M., Brüggen, M., & Begelman, M. C. 2004a, *ApJ*, 611, 158

Ruszkowski, M., Brüggen, M., & Begelman, M. C. 2004b, *ApJ*, 615, 675

Sand, D. J., Treu, T., & Ellis, R. S. 2002, *ApJ*, 574, L129

Sand, D. J., Treu, T., Smith, G. P., & Ellis, R. S. 2004, *ApJ*, 604, 88

Sanderson, A. J. R., Ponman, T. J., Finoguenov, A., Lloyd-Davies, E. J., & Markevitch, M. 2003, *MNRAS*, 340, 989

Sarazin, C. L. 1988, X-ray emission from clusters of galaxies (Cambridge Astrophysics Series, Cambridge: Cambridge University Press, 1988)

Schmidt, R. W., Allen, S. W., & Fabian, A. C. 2004, *MNRAS*, 352, 1413

Soker, N. & Pizzolato, F. 2004, in Galaxies: New Insights from XMM-Newton, and INTEGRAL: 35th COSPAR Scientific Assembly, Paris, France, 18–25 July 2004 (astro-ph/0407229)

Strüder, L. & et al. 2001, *A&A*, 365, L18

Struble, M. F. & Rood, H. J. 1999, *ApJS*, 125, 35

Sun, M., Jones, C., Murray, S. S., Allen, S. W., Fabian, A. C., & Edge, A. C. 2003, *ApJ*, 587, 619

Tamura, T., Kaastra, J. S., Peterson, J. R., Paerels, F. B. S., Mittaz, J. P. D., Trudolyubov, S. P., Stewart, G., Fabian, A. C., Mushotzky, R. F., Lumb, D. H., & Ikebe, Y. 2001, *A&A*, 365, L87

Tozzi, P. & Norman, C. 2001, *ApJ*, 546, 63

Tozzi, P., Scharf, C., & Norman, C. 2000, *ApJ*, 542, 106

Tyson, J. A., Kochanski, G. P., & dell'Antonio, I. P. 1998, *ApJ*, 498, L107+

Vikhlinin, A., Markevitch, M., Murray, S. S., Jones, C., Forman, W., & Van Speybroeck, L. 2004, *A&A*, in press (astro-ph/0412306)

Vikhlinin, A., McNamara, B. R., Forman, W., Jones, C., Quintana, H., & Hornstrup, A. 1998, *ApJ*, 502, 558

Voigt, L. M. & Fabian, A. C. 2004, *MNRAS*, 347, 1130

Voit, G. M. & Ponman, T. J. 2003, *ApJ*, 594, L75

Wise, M. W., McNamara, B. R., & Murray, S. S. 2004, *ApJ*, 601, 184

Zhang, Y.-Y., Finoguenov, A., Böhringer, H., Ikebe, Y., Matsushita, K., & Schuecker, P. 2004, *A&A*, 413, 49

Zhao, H. 1996, *MNRAS*, 278, 488